Water Air Soil Pollut (2023) 234:619
https://doi.org/10.1007/s11270-023-06638-5

Efficient Activation of Persulfate by TiO_2/g-C_3N_4 Composite for Degradation of Acetaminophen Under Visible Light

Huize Jiang · Jinge Yang · Xinxin Wang · Aihong Wang · Yuzhi li · Jinyu Wang

Received: 30 June 2023 / Accepted: 8 September 2023 / Published online: 18 September 2023

Abstract The massive use of acetaminophen (APAP) poses a potential crisis for humans and the environment. In this paper, the degradation of APAP in aqueous solution was carried out using photocatalytic synergistic persulfate oxidation. To enhance the photocatalytic activity of g-C_3N_4 and thus activate the persulfate ($K_2S_2O_8$, PS) more effectively, the heterojunction photocatalyst TiO_2/g-C_3N_4 (TCN) was prepared by a hydrothermal method. The TCN-PS catalytic system showed a high efficiency for APAP degradation. When the amount of TCN and PS added was 0.6 g/L, the degradation rate of APAP at 10 mg/L was 78.3% after 60 min of illumination. Moreover, the TCN-PS catalytic system was effective in removing organic pollutants in acidic, neutral, and weakly alkaline environments. The radical quenching experiment results indicate that both sulfate radicals (SO_4^{-}•) and hydroxyl radicals (•OH) are involved in the degradation reaction. After five cycles, the TCN-PS catalytic system still has stable catalytic activity.

Keywords Photoactivation · Visible light · Persulfate · g-C_3N_4 · TiO_2 · Environmental purification

H. Jiang (✉) · J. Yang · X. Wang · A. Wang · Y. li · J. Wang
State Key Laboratory of NBC Protection for Civilian, Beijing 102205, China
e-mail: 779800808@qq.com

1 Introduction

Persulfate oxidation technology is an advanced oxidation technique to degrade pollutants (Dombrowski et al., 2018). In comparison to advanced oxidation techniques based on •OH, persulfate oxidation has more application prospects since $^{SO4-}$• have considerable redox potential (2.5–3.1 V), a longer half-life, and a wider range of pH adaptation (Matzek & Carter, 2016; Wang & Wang, 2018; Zhou et al., 2019). Researchers have traditionally concentrated on finding effective techniques to activate PS fast to produce SO_4^{-}• when persulfate oxidation technology is used(Xu et al., 2018).

For the activation of PS, researchers have developed methods such as alkali activation, thermal activation, transition metal ion activation, ultrasonic activation, and UV irradiation activation (Do et al., 2010; Fordham & Williams, 1951; Furman et al., 2010; Wang et al., 2014). However, all these activation methods have limitations and are not suitable for large-scale application. Among them, alkaline activation creates a strong alkaline environment, which can be harmful to the environment; thermal activation requires a lot of energy; transition metal ion activation does not require energy, but the introduced metal ions can cause secondary pollution and require secondary treatment; and ultrasonic activation, like thermal activation, requires a lot of energy (Chen et al., 2019; Li et al., 2022; Waclawek et al., 2017). In comparison to previous activation techniques, UV irradiation

activation uses less energy, but the low UV content of sunlight prevents the widespread use of this technique (Ghaly et al., 2017; Zhang et al., 2019b).

Based on the advantages of green sunlight and energy savings, researchers attempted to use sunlight to activate PS (Zhang et al., 2019a). The introduction of photocatalysts into the catalytic system is one of the methods available to improve the utilization of sunlight and the activation efficiency of PS (Ming et al., 2022). The first investigation on the degradation of organic matter utilizing photocatalyst-activated PS under visible light was published in 2011 by Zhou et al. (Zhou et al., 2011). Since then, the reports of photocatalytically activated PS degradation of organic pollutants have gradually increased (Zhang et al., 2020). Currently, photocatalysts used to activate PS can be divided into two types: metal-based and non-metal-based photocatalysts (Tian et al., 2022). Between them, metal-based photocatalysts have been more frequently reported, including Ti, Bi, Fe, Co, Mn, and Mo (Chen et al., 2020; Gao et al., 2016; Lim, 2018; Saputra et al., 2013; Yang et al., 2019b). In contrast, activation of PS by non-metallic photocatalysts has been reported less frequently and is mainly focused on g-C_3N_4 (Tao et al., 2015). g-C_3N_4 is an emerging photocatalyst for treatment of organic pollutants (Li et al., 2018). However, the bulk g-C_3N_4 prepared by traditional thermal condensation has some inherent limitations, including a high recombination rate of photogenerated electron–hole pairs, a slow charge carrier transfer rate, and low electronic conductivity, all of which severely limit its practical application (Li et al., 2018). Garadkar et al. prepared g-C_3N_4-TiO_2 heterojunction catalyst by in situ gel sol method (Kuldeep et al., 2021). Due to the effective electron–hole charge separation and extended optical property, the g-C_3N_4-TiO_2 acquired a noticeable enhancement of photocatalytic activity which is double for methyl orange degradation than TiO_2. To enhance the photocatalytic activity of g-C_3N_4 and thus activate the PS more effectively, elemental doping and compounding with other catalysts are two common means (Lin & Zhang, 2017; Zhou et al., 2016). Although some work has been carried out by researchers in this area, there is still less research available compared to the activation of PS by metal-based catalysts. Further research is needed on how to modify g-C_3N_4 for the purpose of effectively activating PS to degrade contaminants.

APAP is a typical pharmaceutical compound that can be used to relieve pain and fever symptoms (Zhang et al., 2015). With the widespread use of APAP, it has become one of the compounds with the highest detection rate in natural water bodies (Kim et al., 2012). Research has shown that through the enrichment of the food chain in ecosystems, APAP in natural water bodies may have an impact on human health (Zhang et al., 2017). Zhang et al. used a biological method to treat APAP and completely degraded 2000 ppm APAP in 116 h. Although the biological method can effectively degrade APAP, it is too time-consuming and inefficient (Zhang et al., 2013).

In this paper, TiO_2/g-C_3N_4 (TCN) composite photocatalysts were prepared by a hydrothermal method. The TCN was used to activate PS under visible light irradiation to synergistically degrade the APAP in an aqueous solution. The effects of catalytic system composition, catalyst dosage, and chemical environment on the degradation effect were investigated. Free radical trapping experiments were designed to explore the main active substances in TCN-PS catalytic system for the degradation of organic pollutants. The stability and recyclability of the catalysts were evaluated through cycling experiments. We hope that this work will provide a strategy for the activation of PS and the degradation of organic pollutants in aqueous solution.

2 Experimental Section

2.1 Chemicals

Melamine ($C_3H_6N_6$, 99%) and tert-butyl alcohol ($C_4H_{10}O$, 99.5%) were purchased from Aladdin Biochemical Technology Co., Ltd (Shanghai, China). Titanium butoxide (CHO_4Ti, 99.0%), ethanol absolute (C_2H_6O, 99.5%), persulfate ($K_2S_2O_8$, 99.5%), sodium hydroxide (NaOH, 95%), and acetamidophenol ($C_8H_9NO_2$, 99%) were purchased from Shanghai Macklin Biochemical Co., Ltd (Shanghai, China). Hydrochloric acid (HCl, AR) was purchased from Sichuan Xilong Science Co., Ltd (Chengdu, China).

Synthesis of g-C_3N_4: g-C_3N_4 was prepared by thermal sintering (Zou et al., 2020). The specific experimental process is as follows: 10 g of melamine was placed into a ceramic ark and transferred to a muffle furnace, and then heated to a certain temperature of 550 °C for 2 h at a heating rate of 5 °C min^{-1} in air

atmosphere. Finally, g-C_3N_4 was obtained after natural cooling to room temperature.

2.2 Synthesis of TCN

TCN composite photocatalysts were prepared by the hydrothermal method. The specific experimental procedure is as follows: A certain mass of g-C_3N_4 (12.30, 6.92, 4.56, 3.23, 1.19, and 0.15 g), 10 mL of anhydrous ethanol, and 6 mL of glacial acetic acid were added to 20 mL of anhydrous ethanol and sonicated for 30 min to obtain solution A. Under vigorous stirring, 2 mL of glacial acetic acid and 6.5 mL of n-butyl titanate were added sequentially to 20 mL of anhydrous ethanol to obtain solution B. Solution B was then slowly dripped into solution A under vigorous stirring to obtain a mixed solution. The resulting mixture was sonicated for 5 min and then reacted in a PTFE autoclave at 160 °C for 20 h. The mass of TiO_2 in all TCNs was 1.52 g, calculated from the amount of n-butyl titanate added. Finally, TCN with different mass ratios was obtained after centrifugation, alcohol washing, and drying. TCN with mass fraction of 11%, 18%, 25%, 32%, 56%, and 91% TiO_2 was named as TCN_{11}, TCN_{18}, TCN_{25}, TCN_{32}, TCN_{56}, and TCN_{91}, respectively.

2.3 Characterization of Photocatalyst

The XRD spectra of g-C_3N_4, TiO_2 and TCN were obtained by an X-ray spectrometer (Bruker D8 Advance). The UV–Vis diffuse reflectance spectra of g-C_3N_4, TiO_2, and TCN were measured using a UV/Vis/spectrophotometer (Shimadzu UV-3600). The chemical compositions and valence band of the TCN were detected by X-ray photoelectron spectroscopy (XPS, Thermo Scientific K-Alpha). The XPS sample preparation method is as follows: first, press an appropriate amount of powder sample into flakes, then apply conductive adhesive to the sample disk, and then send it to the instrument sample room for analysis. The bonding energies of O, N, and Ti elements were calibrated according to C1s 284.8 eV. Photoluminescence spectroscopy (PL) was recorded on an Edinburgh FLS1000. The morphology and microstructure of g-C_3N_4 and TCN were observed by scanning electron microscopy (ZEISS GeminiSEM 300) and transmission electron microscopy (JEOL JEM-2100Plus). The IR spectra of TiO_2, g-C_3N_4 and TCN were determined using a FTIR spectrometer (Thermo Scientific Nicolet iS5).

2.4 Photocatalytic Degradation of APAP

The catalytic system of TCN-PS was constructed by combining the TCN with PS, which was then used to degrade APAP in an aqueous solution under visible light irradiation to evaluate the catalytic activity of TCN-PS. The visible light source is provided by a xenon lamp (500 W) fitted with a 420-nm filter and was 5 cm from the beaker. Moreover, circulating water was utilized as a thermostat to regulate the reaction system's temperature. A total of 10–50 mg TCN was dispersed in 50 mL solution of a certain concentration of APAP, then stirred in the dark for 30 min to reach adsorption–desorption equilibrium, and finally, 10–50 mg of PS was added. The light source was turned on, and photocatalytic degradation was started. A total of 1 mL of sample was taken at regular intervals and promptly quenched with 0.1 mL of methanol as a free radical quencher. The sample was then filtered through a 0.45 μm PTFE membrane and kept storage at a low temperature for 1–5 days. A total of 0.1 M HCl solution and 0.1 M NaOH solution were used to adjust the pH of the solution while investigating the effect of starting pH on pollutant degradation. When carrying out quenching experiments, a certain mass of quencher was added to the system before the TCN catalyst was added. The concentration of APAP in the water samples was detected by high performance liquid chromatography (HPLC, UltiMate 3000), equipped with a reversed-phase C18 column at 21.0 °C, and a diode array detector set at 230 nm. The mobile phase, used for elution, was water–methanol (V:V = 40%:60%) with a flow rate of 1.0 mL min^{-1}. The batch degradation experiments were performed with 2 ~ 3 times to obtain average values with standard deviations.

3 Result and Discussion

Firstly, the effect of TCN composition on the catalytic performance of TCN-PS was investigated, and the results are shown in Fig. 1a. To more intuitively analyze APAP degradation, the degradation rate of APAP was fitted using Eq. 1.

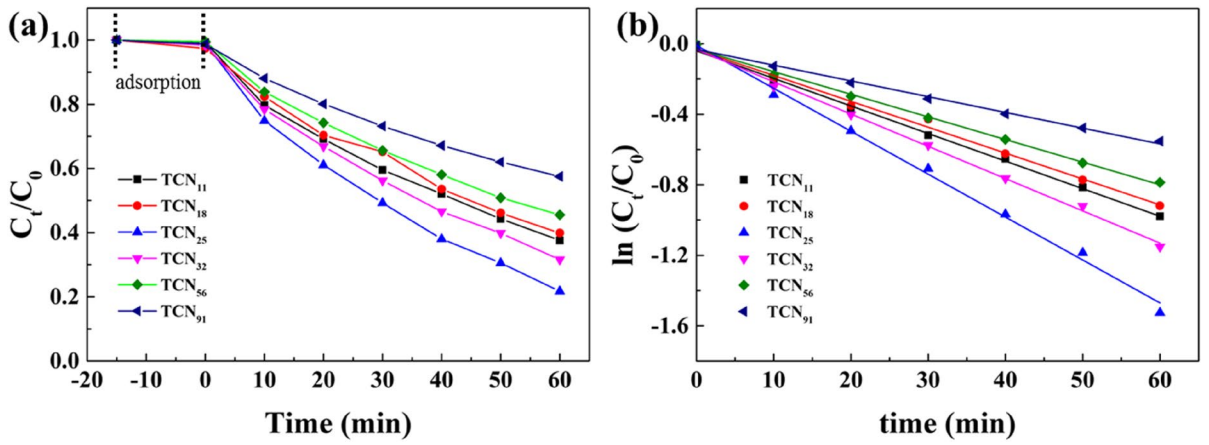

Fig. 1 **a** Effect of the TCN composition on APAP degradation. **b** The rate constant k_{obs} of different TCN composition. Conditions: $(APAP)_0 = 10$ mg/L, $(catalyst)_0 = 0.6$ g/L, $(PMS)_0 = 0.6$ g/L, the initial pH = 7

$$\ln(C_t/C_0) = -k_{obs}t \quad (1)$$

where k_{obs} is the observed pseudo-first-order rate constant (min^{-1}) in APAP degradation.

As can be seen in Fig. 1a, the concentration of APAP was reduced by less than 2% after 30 min of adsorption. The results show that the adsorption performance of different TCN components on APAP does not change significantly. After 60 min of illumination, the degradation rate of APAP by TCN-PS constructed with TCN_{11}, TCN_{18}, TCN_{25}, TCN_{32}, TCN_{56}, and TCN_{91} were 62.4%, 60.1%, 78.3%, 68.4%, 54.5%, and 42.5%, respectively. The results reveal that the removal efficiency of APAP by TCN-PS differs depending on the TCN composition. Among them, the k_{obs} of APAP is the highest when the content of TiO_2 in TCN is 25% (Fig. 1b). Table 1 lists the kinetic parameters for the degradation of APAP by TCN-PS with different compositions of TCN. With the increase of TiO_2 content in TCN, the k_{obs} was 0.0156, 0.0147, 0.0243, 0.0183, 0.0128, and 0.0089 min^{-1}. The results show that the TCN-PS catalytic system constructed with TCN_{25} containing 25% TiO_2 exhibits the best degradation of APAP in aqueous solution. This may be attributed to the fact that when the TiO_2 content in TCN was too high, g-C_3N_4 produced fewer photoactivated hole-electron pairs by light, whereas when the TiO_2 content was low, the photogenerated electrons produced by g-C_3N_4 by light could not be transferred to TiO_2 in time. Therefore, TCN_{25} was selected for further studies.

The microscopic morphology of g-C_3N_4 and TCN_{25} was further observed using TEM, as shown in Fig. 2a-d. It can be seen that g-C_3N_4 exhibits a folded planar state, and no regular lattice arrangement is observed. In contrast, in addition to amorphous g-C_3N_4, spindle TiO_2 particles with sizes of several nanometers and tens of nanometers can be observed on the surface of g-C_3N_4 in the HRTEM diagram of TCN. The TiO_2 particle lattice spacing of $d = 0.35$ nm corresponds to the (101) crystal plane of anatase TiO_2 (Huo et al., 2019). SEM and TEM analyses show that TiO_2 in the anatase phase can still be obtained by hydrothermal reaction in the presence of g-C_3N_4 and that the g-C_3N_4 and TiO_2 particles are uniformly dispersed in TCN. The SEM image of TCN_{25} is shown in Fig. 1e. As can be seen from Fig. 2e, TCN_{25} is composed of particles with sizes ranging from tens to hundreds of nanometers stacked together.

Table 1 Kinetic parameters for the degradation of APAP by TCN-PS with different compositions of TCN

Catalyst	TCN_{11}-PS	TCN_{18}-PS	TCN_{25}-PS	TCN_{32}-PS	TCN_{56}-PS	TCN_{91}-PS
R^2	0.9955	0.9941	0.9947	0.9971	0.9965	0.9946
k_{obs} (min^{-1})	0.0156	0.0147	0.0243	0.0183	0.0128	0.0089

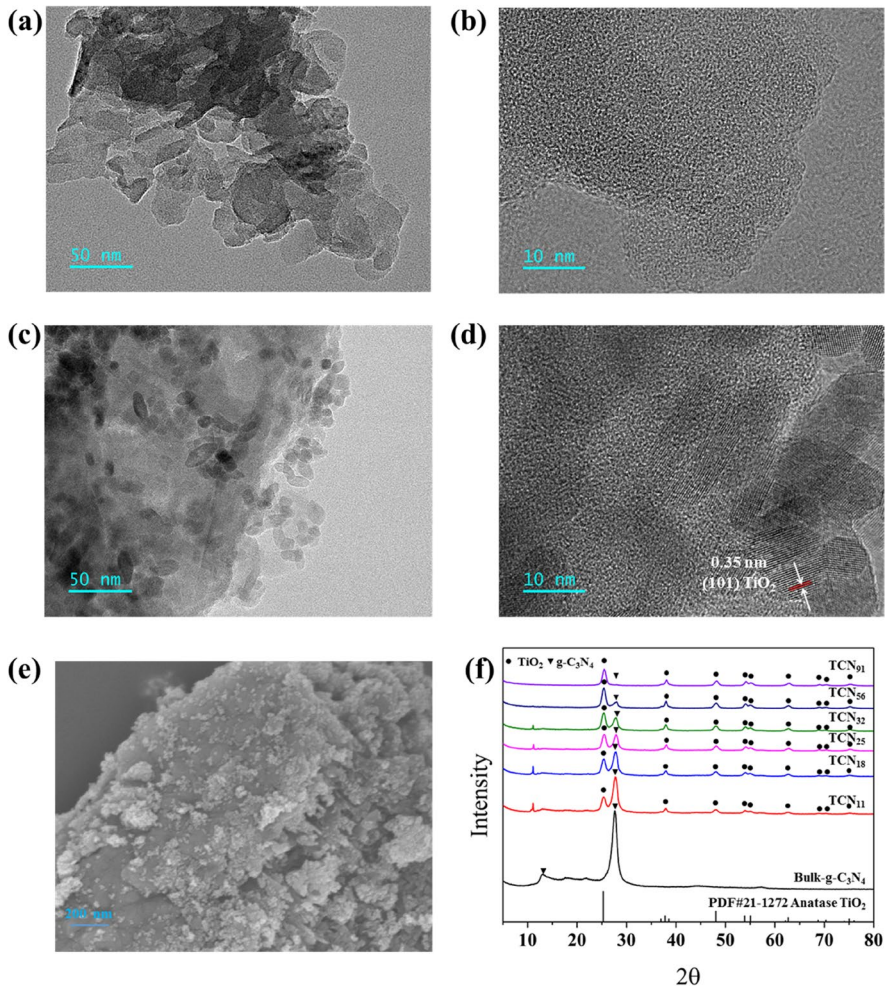

Fig. 2 TEM images of g-C_3N_4 (**a**, **b**) and TCN (**c**, **d**). SEM (**e**) images of TCN. **f** XRD spectra of g-C_3N_4 and TCN

The crystal structures of g-C_3N_4 and different components of TCN were investigated using XRD, and the results are shown in Fig. 2f. The characteristic diffraction peaks located at 13.1° and 27.6° can be observed in the XRD spectrum of g-C_3N_4, corresponding to the (002) and (100) crystal planes of g-C_3N_4, respectively, indicating the successful conversion of the precursor melamine to g-C_3N_4 under the set conditions (Li et al., 2018). In all the XRD spectra of the TCN, characteristic diffraction peaks belonging to the anatase phase TiO_2 can be observed at 25.3°, 37.9°, 48.1°, 54.0°, 55.1°, 62.6°, 68.8°, 70.4°, and 75.0° (Pelaez et al., 2012), indicating that anatase phase TiO_2 can still be obtained by hydrothermal methods in the presence of g-C_3N_4 and is consistent with previous TEM analyses. In addition, characteristic diffraction peaks belonging to g-C_3N_4 at 27.6° were clearly observed in the XRD spectra of all the TCNs except TCN_{91}, indicating that g-C_3N_4 remains stable after hydrothermal treatment. In the XRD spectrum of TCN_{91}, the characteristic diffraction peak at 26.9° was weak. The reason why the peak height at 27.6° belonging to g-C_3N_4 gradually decreases is because the content of g-C_3N_4 gradually decreases with the increase in TiO_2 content (Yang et al., 2019a).

To further determine the composition of the TCN_{25}, Fourier transform infrared spectroscopy was used to obtain information on the functional groups in the catalyst, and the results are shown in Fig. 3a. A characteristic peak located at 446.9 cm^{-1} belonging to anatase TiO_2 can be observed in the infrared spectrum of TiO_2, which is generated by the stretching vibrations of the Ti–O–Ti bond and the Ti–O bond (Tan et al., 2018a). In addition, the broad peaks located between 3000.0 and 3500.0 cm^{-1} and characteristic peaks generated by O–H bond bending and stretching vibrations near

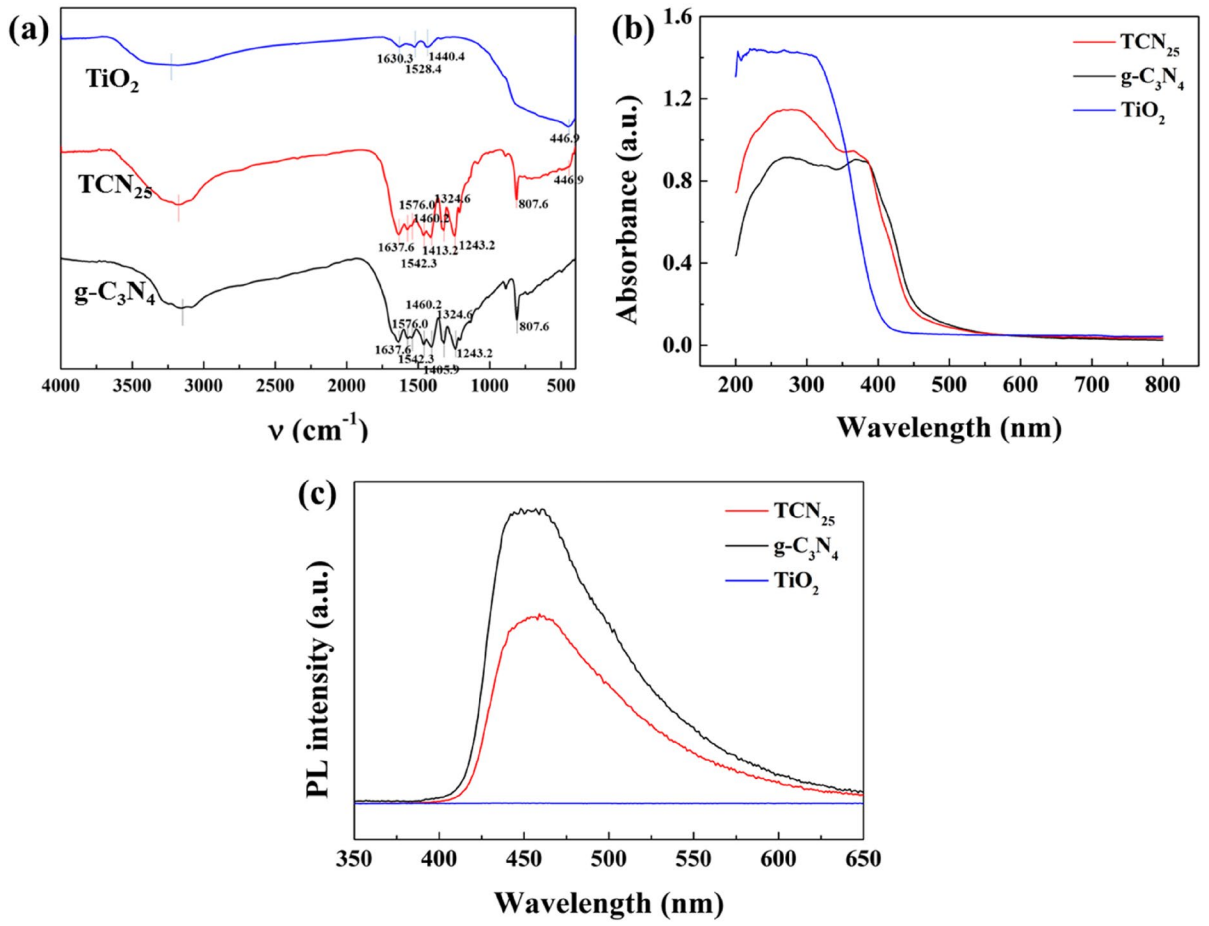

Fig. 3 **a** FTIR, **b** Uv–Vis absorption, and **c** PL spectra of g-C_3N_4, TiO_2, and TCN_{25}

1528.4 cm^{-1} can be observed, which originate from water and hydroxyl radicals adsorbed on the TiO_2 surface (Tan et al., 2018a). In contrast, more absorption peaks can be observed in the spectrum of g-C_3N_4. Among them, the absorption peak at 807.6 cm^1 is generated by stretching vibrations of the 3-s-triazine ring system; the peaks at 1243.2 to 1637.6 cm^{-1} are generated by C–N and C=N bonding vibrations, and the broad peaks at 3000.0 to 3500.0 cm^{-1} are generated by the C–NH_2, C–NH at the edge of g-C_3N_4, and the –OH tensile vibration of H_2O adsorbed on the surface of g-C_3N_4 (Lin et al., 2016). The characteristic peaks belonging to both TiO_2 and g-C_3N_4 can be observed in the TCN spectra, indicating that the TCN contains both TiO_2 and g-C_3N_4, which is consistent with the XRD analysis results.

Figure 3b shows the UV–Vis absorption spectra of TiO_2, g-C_3N_4, and TCN_{25}. As can be observed, TiO_2 has a very poor absorption in the visible region with an absorption sideband of 390 nm (Pelaez et al., 2012). In contrast, the absorption of g-C_3N_4 in the ultraviolet region is slightly weak, but its absorption in the visible region is much higher than that of TiO_2. After compounding TiO_2 with g-C_3N_4, the UV–Vis absorption spectrum of the TCN_{25} is similar to that of g-C_3N_4, showing high absorption in both the UV and visible regions.

The separation efficiency of photogenerated electron–hole pairs was determined using photoluminescence spectroscopy. Figure 3c gives the PL spectra of TiO_2, g-C_3N_4, and TCN_{25}. In the g-C_3N_4 PL spectrum, a significant emission peak around 460 nm was

noticed, which can be attributed to the intrinsic electronic transition (Sudrajat, 2018). After being composited with TiO_2, the intensity of the emission peak near 460 nm was significantly lowered. Comparative result shows that the recombination of photogenerated carriers in TCN_{25} is significantly suppressed, which is due to that the photo-induced electrons are transferred from g-C_3N_4 to TiO_2 via the interfacial heterojunction (Tan et al., 2018b). Furthermore, no apparent emission peak at 460 nm was seen for pure TiO_2, which is consistent with prior research (Zada et al., 2018).

To investigate the catalytic activity of different catalytic systems, the removal of APAP by PS, TCN_{25}, g-C_3N_4-PS, and TCN_{25}-PS was compared, and the results are shown in Fig. 4a. It can be seen that when using PS and TCN_{25} alone to degrade APAP, the removal of APAP after 1 h of visible light irradiation was only 9.5% and 20.1%, respectively. In contrast, when PS and TCN_{25} were used to synergistically degrade APAP under visible light irradiation, the degradation rate of APAP increased significantly, reaching 78.3%. In contrast, the degradation rate of APAP increased noticeably and reached 78.3% when the TCN_{25}-PS catalytic system was employed to degrade APAP under visible light irradiation. The results show that under visible light irradiation, TCN_{25} and PS interact to produce more active substances, with a subsequent increase in the removal of APAP. In addition, when g-C_3N_4-PS and TiO_2-PS was used to degrade APAP, only 19.3% and 31.4% of APAP were removed after 60 min of light, which was much lower than the degradation rate of APAP by TCN_{25}-PS. The k_{obs} of APAP by g-C_3N_4-PS, TiO_2-PS, and TCN_{25}-PS was 0.003, 0.0058, and 0.0243 min^{-1}, respectively (Fig. 4b). PL analyses show that the recombination of photogenerated carriers in TCN_{25} is significantly suppressed by the composite TiO_2. Subsequently, more free electrons in TCN_{25} can synergistically activate PS to produce reactive oxidizing species for faster APAP degradation.

The dosage of photocatalyst and PS has a direct impact on the yield of active species, whereas the concentration of active species has a direct impact on the removal of organic pollutants. Therefore, the effects of TCN and PS dosages on the catalytic performance of TCN-PS were discussed. Firstly, the effect of TCN dosage on the catalytic performance of TCN-PS was investigated at a fixed PS dosage of 0.6 g/L and an initial APAP concentration of 10 mg/L, and the results are shown in Fig. 4c. When the TCN dosage was increased from 0.2 to 0.6 g/L, the degradation rate of APAP increased significantly, from 43.3 to 78.3%. However, as the TCN dosage was further increased to 1 g/L, the k_{obs} of APAP decreased, from 0.0243 to 0.0184 min^{-1}, as shown in Fig. 4d. The study shows that the change in the k_{obs} of APAP is divided into two phases with increasing TCN dosage. When the TCN dosage was low, the higher TCN concentration generated more photoactivated hole-electron pairs, enhanced the activation efficiency of the PS, and sped up the rate of APAP removal (Gul et al., 2020). However, when the TCN dosage was too high, the activation efficiency of the PS gradually stabilizes due to a fixed PS dosage in the system. On the other hand, the high concentration of TCN in solution has the potential to hinder light propagation, preventing a portion of the TCN catalyst from being irradiated by light, and the photoactivated hole-electron pairs in the system will also be reduced, leading to a reduction in the k_{obs} (Ghasemi et al., 2016).

Then, with a fixed TCN dosage of 0.6 g/L and a starting APAP concentration of 10 mg/L, the effect of PS dosage on APAP degradation was explored, and the results are shown in Fig. 4e. It is clear that as the PS dosage increases, the rate of APAP degradation initially rises and then falls. At PS dosages of 0.2, 0.4, 0.6, 0.8, and 1.0 g/L, the degradation rates of APAP were 62.7%, 64.7%, 78.3%, 73.6%, and 67.9%, respectively. When the PS dosage was increased from 0.2 g to 0.6 g/L, the SO_4^{-}• produced by activation in unit time increased as the concentration of PS in the system increased, which was reflected in the increasing of the k_{obs} (Zhang et al., 2020). However, since the photocatalyst is pitched at a fixed amount, the number of photoactivated hole-electron pairs produced per unit time is limited, and the upper limit of the amount of PS that can be activated per unit time is also limited, the k_{obs} does not continue to increase with higher PS concentration (Zhang et al., 2020). In addition, excessive PS in the system will react with SO_4^{-}• to eliminate some active species (Zhang et al., 2020). Therefore, the catalytic activity of TCN-PS not only does not increase but also decreases when the dosage of PS was too high. Among them, the highest k_{obs} of APAP by TCN-PS was 0.0243 min^{-1} at a PS dosage of 0.6 g/L, as shown in Fig. 4f.

In addition to the composition of the catalytic system, the external chemical environment, such as the starting concentration of the APAP and the pH of the

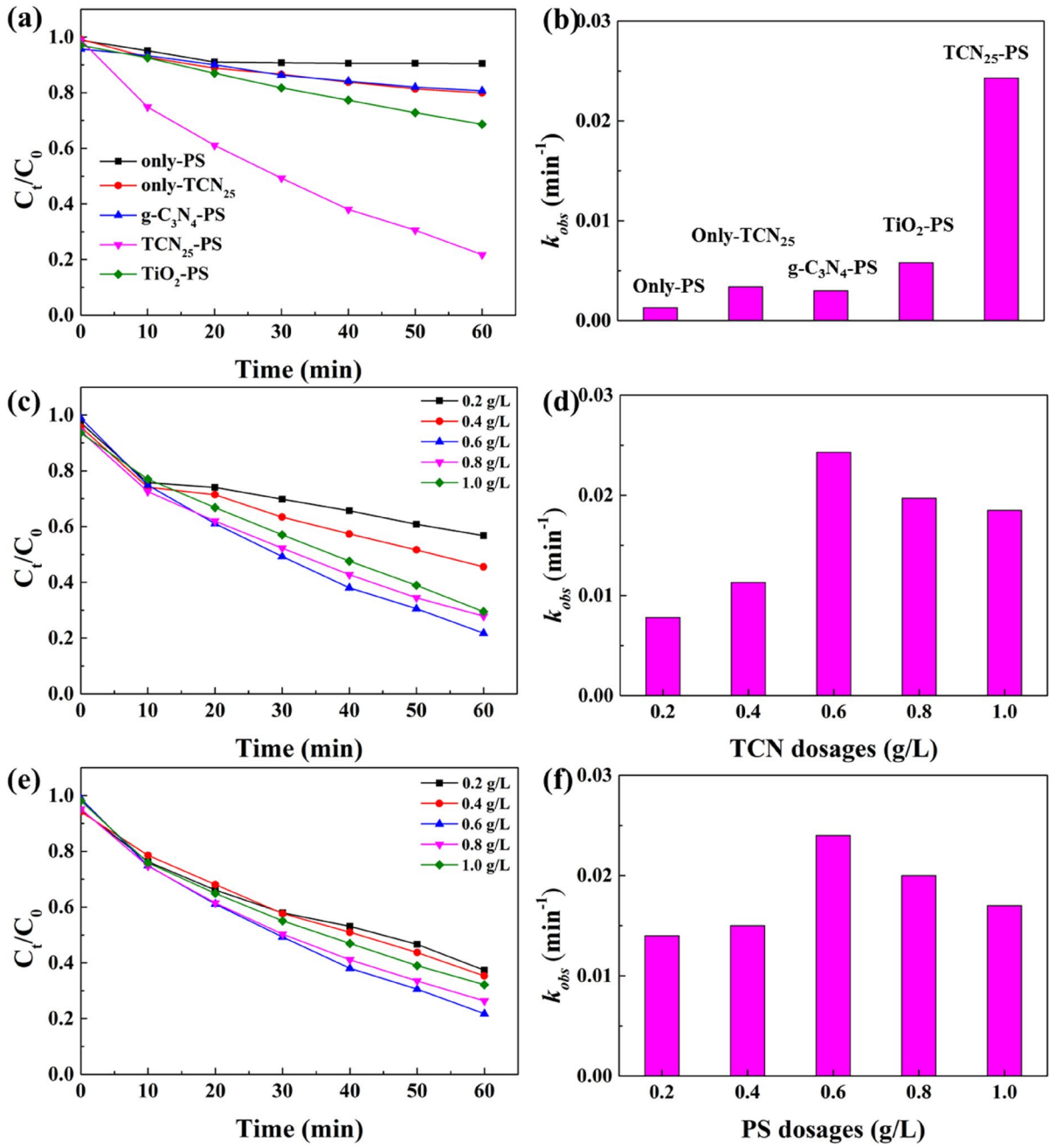

Fig. 4 Effect of the catalytic system (**a**, **b**), TCN dosage (**c**, **d**), and PS dosage (**e**, **f**) on APAP degradation. Conditions: $(APAP)_0 = 10$ mg/L, $(catalyst)_0 = 0.6$ g/L, $(PMS)_0 = 0.6$ g/L, the initial pH = 7

starting solution, will also directly affect the removal effect of the APAP. By adjusting the pH of the starting solution with 0.1 M hydrochloric acid and sodium hydroxide, the impact of initial pH on the catalytic performance was examined, and the results are depicted in Fig. 5a. The initial concentration of APAP is 10 mg/L, and the dosage of TCN and PS is 0.6 g/L. It can be seen that the acidity and alkalinity of the initial solution have a significant effect on the degradation rate of APAP. The degradation rates of APAP

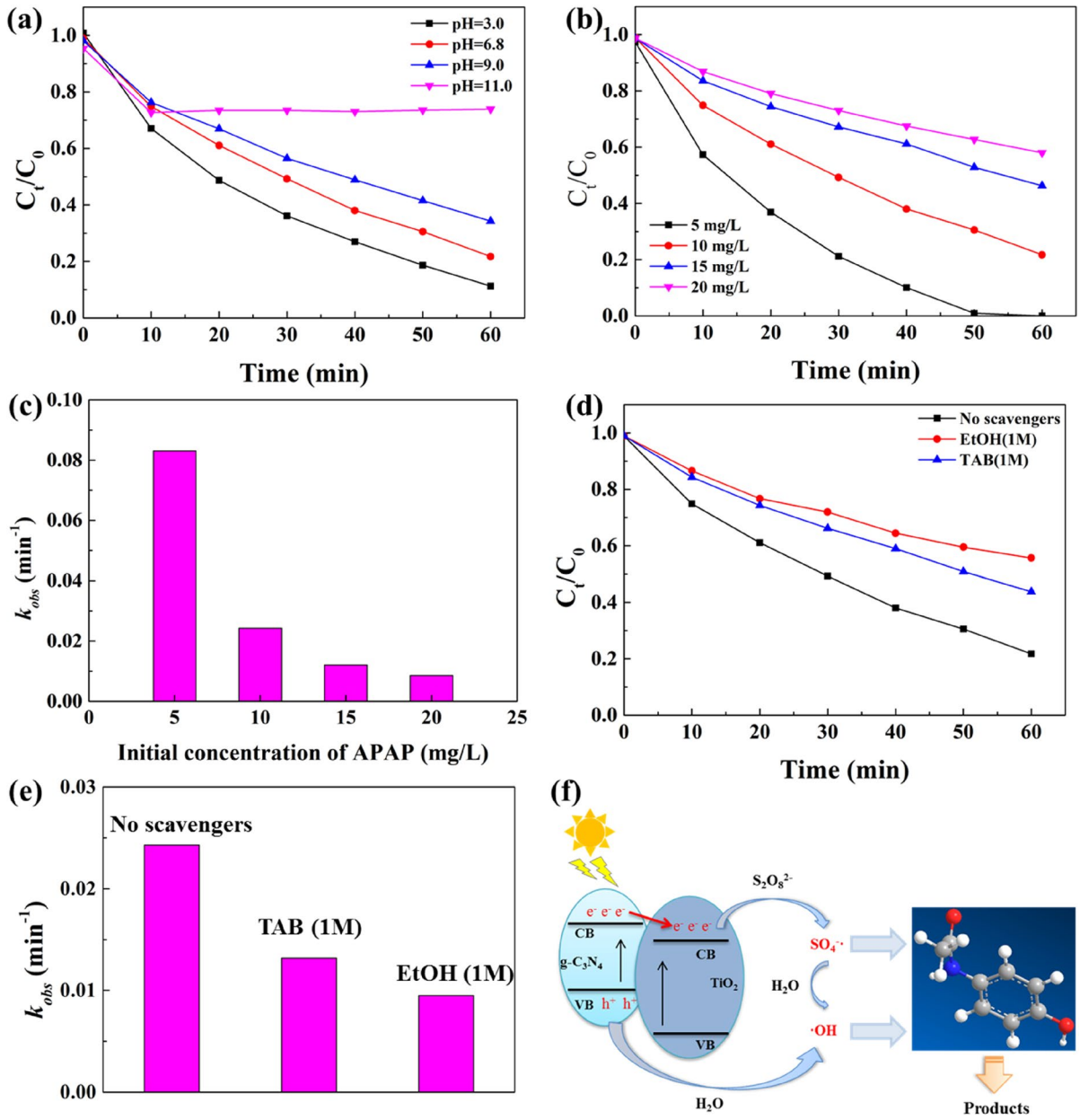

Fig. 5 Effect of initial pH of solution (**a**), initial concentration of APAP (**b**, **c**), and scavengers (**d**, **e**) on APAP degradation, a possible mechanism for the degradation (**f**). Conditions: $(APAP)_0 = 10$ mg/L, $(catalyst)_0 = 0.6$ g/L, $(PMS)_0 = 0.6$ g/L, the initial pH = 7

were 88.7%, 78.3%, 65.7%, and 26.1% for initial solution pH values of 3.0, 6.8, 9.0, and 11.0, respectively. The results show that TCN-PS is effective in degrading APAP in aqueous solutions in acidic, neutral, and weak alkaline environments. However, under the strong alkali environment, the degradation rate of APAP decreased significantly. This is most likely because as the pH rises, the SO_4^{-}• in the system gradually converts to the less oxidizing •OH, and the oxidation potential of •OH gradually decreases, both of which inhibit APAP degradation (Gul et al., 2020).

The effect of initial APAP concentrations on the removal of APAP was studied by fixing the TCN and PS dosages at 0.6 g/L and an initial pH of 6.8, as

shown in Fig. 5b, c. It can be seen that APAP with a starting concentration of 5 mg/L was totally deteriorated at a rate of 0.0831 min^{-1} after 60 min of light illumination. After the initial concentration of APAP was increased to 10, 15, and 20 mg/L, the degradation rate of APAP was 78.3%, 53.7%, and 42.0%, respectively, with *kobs* of 0.0243, 0.0121, and 0.0086 min^{-1} in that order. The results show that as the initial concentration of APAP increases, its removal efficiency decreases gradually. This is because for a given amount of TCN and PS, the number of active species produced in the system remains constant. The probability of a single APAP being trapped by active species gradually declines as the initial concentration of APAP increases, and the efficiency of degradation similarly decreases gradually. Furthermore, the intermediate products of APAP degradation will react with the active species and be oxidized further. More APAP and its byproducts would exist in the solution with the increasing of initial APAP concentration, thus there would be a competition between active species and contaminants and its intermediates, slowing down the degradation process (Zhang et al., 2020).

A free radical capture experiment was designed to investigate the active species of TCN-PS degrading APAP. Specifically, catalytic degradation experiments were carried out using ethanol as a trapping agent for •OH and SO_4^{-}• and tert-butanol as a trapping agent for •OH (Zhou et al., 2020), with the results shown in Fig. 5d, e. The initial concentration of APAP is 10 mg/L, the dosage of TCN and PS is 0.6 g/L, and the concentration of ethanol and tert-butanol is 1 M. It can be seen that the addition of ethanol and tert-butanol reduced the removal of APAP to 44.3% and 56.2%, respectively, both lower than the 78.3% without the addition of scavengers. After adding tert-butyl alcohol, the k_{obs} was somewhat inhibited and decreased from 0.0243 to 0.0132 min^{-1}, indicating that •OH is one of the active species in the TCN-PS system. The inhibition of APAP degradation was more pronounced with ethanol than with tert-butanol, lowering the k_{obs} to 0.0095 min^{-1}. The results reveal that, in addition to •OH, there is SO_4^{-}• with a higher oxidation ability in the TCN-PS system.

Figure 5f depicts a probable reaction mechanism for the degradation of organic pollutants by the TCN-PS catalytic system based on the results of degradation studies and free radical capture experiments. As the photochemical absorption boundaries of TiO_2 and g-C_3N_4 are 390 nm and 450 nm, respectively, only g-C_3N_4 can be excited to generate photogenerated electrons and holes in TCN under visible light irradiation ($\lambda > 400$ nm) (Pelaez et al., 2012; Yang et al., 2019a). The photogenerated electrons swiftly move to TiO_2 CB, enabling charge separation in g-C_3N_4 based on the appropriate energy level difference between the conduction band (CB) edge of g-C_3N_4 and TiO_2 (Wang et al., 2018; Yang et al., 2013). Subsequently, the photogenerated electrons react with the $S_2O_8^{2-}$ in solution to produce SO_4^{-}•. Part of the •OH in the solution comes from the reaction of SO_4^{-}• with H_2O, and the other part comes from the reaction of photogenerated holes with H_2O (Zhang et al., 2020). The concentration of APAP decreased rapidly due to the interaction of SO_4^{-}• and •OH. The degradation efficiency was significantly lower than that of the TCN-PS catalytic system when g-C_3N_4 was utilized to activate the PS, however, as a result of the ease of complexation of the photogenerated electrons and holes of g-C_3N_4 (Yang et al., 2019a).

Cycle degradation experiments were carried out to investigate the cycling stability of the TCN-PS catalytic system, and the results are shown in Fig. 6a. It can be seen that the APAP degradation rates for the five cycles were 78.3%, 68.8%, 61.8%, 60.7%, and 61.2%, respectively. As the number of cycles increased, the APAP degradation rate decreased slightly at first but eventually remained stable at 60%. The changes in the chemical composition of TCN_{25} before and after the reaction were investigated using XPS, and the results are shown in Fig. 6. Three different peaks at 284.80 eV, 285.95 eV, and 288.34 eV were observed in C1s spectrum (Fig. 6b). The peak at 284.80 eV corresponds to the adventitious surface carbon contamination from carbon oxides in the ambient environment (Piao & McIntyre, 2002). The peaks at 285.95 eV and 288.34 eV are attributed to the C=N and $(N)_2$-C=N group (Tan et al., 2018b). Similarly, the N1s spectrum (Fig. 6c) was fitted to three peaks located at 398.83 eV, 400.10 eV, and 401.36 eV, corresponding to the C-N=C, N-$(C)_3$ and N–H groups, respectively (Tan et al., 2018b). In the O 1 s spectrum (Fig. 6d) of TCN_{25}, only two peaks were observed. One peak around 529.83 eV is attributed to the Ti–O bond, and the other peak near 531.66 eV is assigned to the O–H bond (Yang et al., 2019a). Obviously, the Ti 2p spectrum (Fig. 6e) has three peaks at 458.64 eV, 460.00 eV, and 464.34 eV. Among them, the two peaks located

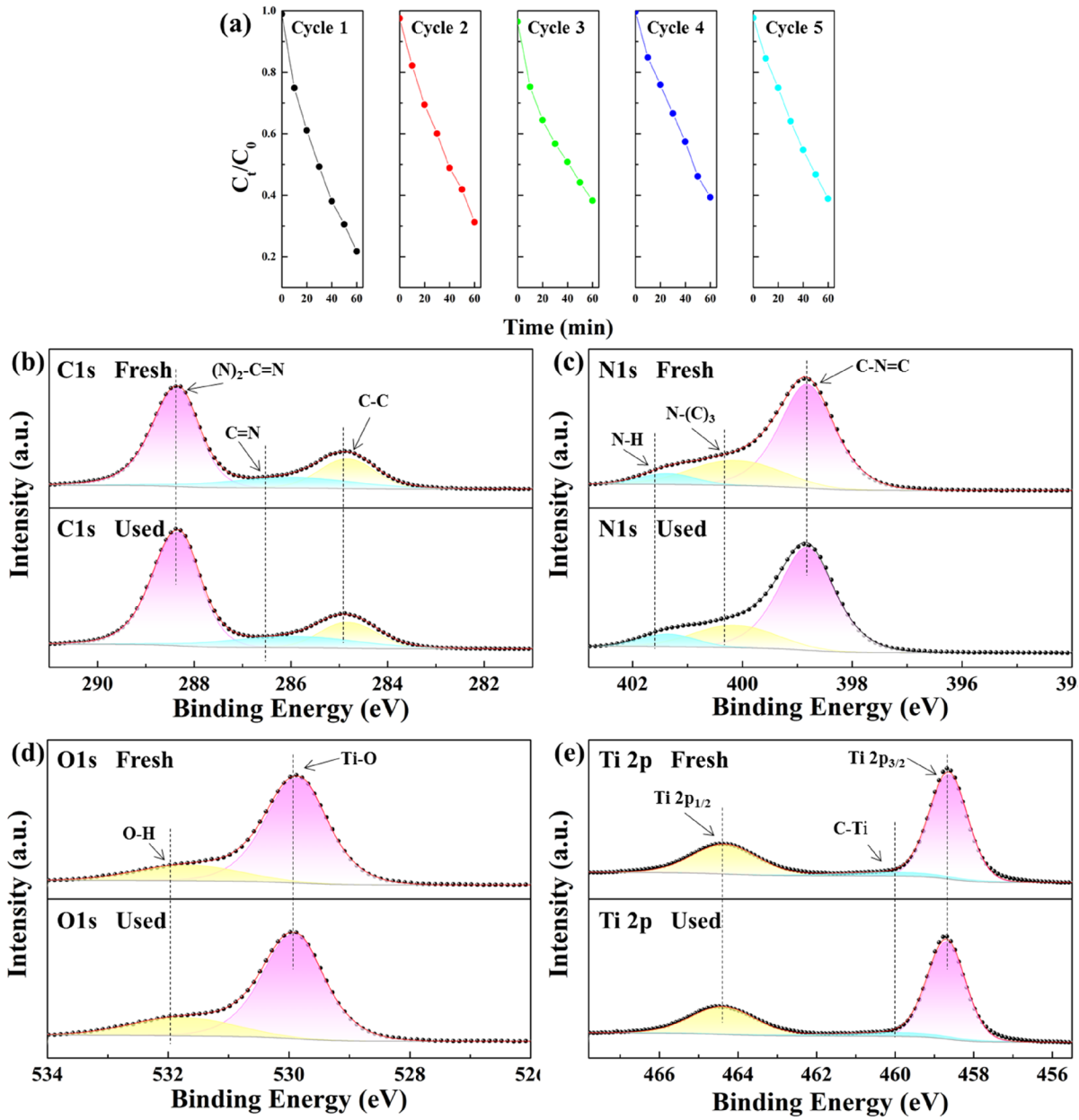

Fig. 6 **a** Results of APAP recycling degradation experiments. XPS spectra of C1s (**b**), N1s (**c**), O1s (**d**), and Ti 2p (**e**) of TCN_{25}. Conditions: $(APAP)_0 = 10$ mg/L, $(catalyst)_0 = 0.6$ g/L, $(PMS)_0 = 0.6$ g/L, the initial pH = 7

around 458.64 eV and 464.34 eV are assigned to Ti $2P_{3/2}$ and Ti $2P_{1/2}$. The peak near 460.00 eV is attributed to C–Ti bond (Yang et al., 2019a). In addition, from Fig. 6b–d, it can be seen that there is no significant change in the binding energy of the characteristic peaks of each element after reaction. Specifically, fitting calculations show that the Ti element in C–Ti is 12.2% and 11.5% of the total Ti element before and after reaction. The results indicate that there is no significant change in the chemical composition of TCN_{25} during the degradation of organic pollutants by activated PS. The results of recycling degradation

experiments and XPS analysis show that TCN is a stable photocatalyst that can be used to activate PS for the degradation of organic pollutants such as APAP.

4 Conclusion

In this paper, TCN heterojunction photocatalysts were prepared using a simple hydrothermal method and successfully activated PS to degrade APAP in an aqueous solution under visible light irradiation. The composite of g-C_3N_4 and TiO_2 inhibited the recombination of photoactivated hole-electron pairs and enhanced the catalytic performance. Thus, compared with TiO_2 and g-C_3N_4, more free electrons in TCN can synergistically activate PS to produce reactive oxidizing species for faster APAP degradation. In TCN_{25}-PS catalyst system, 10 mg/L APAP (50 mL) could be removed 78.3% in 60 min. In addition, the results of the radical quenching experiments show that both •OH and SO_4^{-}• contribute to degrading APAP in TCN-PS catalytic system. The results of recycling experiments indicate that TCN-PS is a stable and effective catalytic system. In summary, inhibiting the recombination of photoactivated hole-electron pairs through composite catalysis can improve the efficiency of g-C_3N_4 in activating PS and the removal efficiency of pollutants. On this basis, enhancing the conductivity of g-C_3N_4 by elemental doping or compounding other catalysts might further enhance its activation efficiency for PS.

Author Contribution Huize Jiang and Jinge Yang contributed to the study conception and design. Material preparation, data collection, and analysis were performed by Huize Jiang, Xinxin Wang, Aihong Wang, Yuzhi Li, and Jinyu Wang. The first draft of the manuscript was written by Huize Jiang, and all authors commented on previous versions of the manuscript. All authors read and approved the final manuscript.

Funding This work was supported by State Key Laboratory of NBC Protection for Civilian (SKLNBC2021-14).

Data availability The data is available from the corresponding author on reasonable request.

Declarations

Ethics Approval Not applicable.

Consent to Participate Not applicable.

Consent for Publication Not applicable.

Competing Interests The authors declare no competing interests.

References

Chen, F., Huang, G., Yao, F., Yang, Q., Zheng, Y., Zhao, Q., & Yu, H. (2020). Catalytic degradation of ciprofloxacin by a visible-light-assisted peroxymonosulfate activation system: Performance and mechanism. *Water research., 173*, 115559.

Chen, L., Hu, X., Cai, T., Yang, Y., Zhao, R., Liu, C., Li, A., & Jiang, C. (2019). Degradation of triclosan in soils by thermally activated persulfate under conditions representative of in situ chemical oxidation (ISCO). *Chemical Engineering Journal, 369*, 344–352.

Do, S.-H., Kwon, Y.-J., & Kong, S.-H. (2010). Effect of metal oxides on the reactivity of persulfate/Fe(II) in the remediation of diesel-contaminated soil and sand. *Journal of Hazardous Materials, 182*, 933–936.

Dombrowski, P. M., Kakarla, P., Caldicott, W., Chin, Y., Sadeghi, V., Bogdan, D., Barajas-Rodriguez, F., & Chiang, S. Y. (2018). Technology review and evaluation of different chemical oxidation conditions on treatability of PFAS. *Remediation Journal, 28*, 135–150.

Fordham, J. W. L., & Williams, H. L. (1951). The persulfate-iron(II) initiator system for free radical polymerizations. *Journal of the American Chemical Society, 73*, 4855–4859.

Furman, O. S., Teel, A. L., & Watts, R. J. (2010). Mechanism of base activation of persulfate. *Environmental Science & Technology, 44*, 6423–6428.

Gao, Y., Zhang, Z., Li, S., Liu, J., Yao, L., Li, Y., & Zhang, H. (2016). Insights into the mechanism of heterogeneous activation of persulfate with a clay/iron-based catalyst under visible LED light irradiation. *Applied Catalysis b: Environmental, 185*, 22–30.

Ghaly, H. A., El-Kalliny, A. S., Gad-Allah, T. A., El-Sattar, N. E. A. A., & Souaya, E. R. (2017). Stable plasmonic Ag/AgCl–polyaniline photoactive composite for degradation of organic contaminants under solar light. *RSC Advances, 7*, 12726–12736.

Ghasemi, Z., Younesi, H., & Zinatizadeh, A. A. (2016). Kinetics and thermodynamics of photocatalytic degradation of organic pollutants in petroleum refinery wastewater over nano-TiO_2 supported on Fe-ZSM-5. *Journal of the Taiwan Institute of Chemical Engineers, 65*, 357–366.

Gul, I., Sayed, M., Shah, N. S., Ali Khan, J., Polychronopoulou, K., Iqbal, J., & Rehman, F. (2020). Solar light responsive bismuth doped titania with Ti^{3+} for efficient photocatalytic degradation of flumequine: Synergistic role of peroxymonosulfate. *Chemical Engineering Journal., 384*, 123255.

Huo, J., Yuan, C., & Wang, Y. (2019). Nanocomposites of three-dimensionally ordered porous TiO_2 decorated with pt and reduced graphene oxide for the visible-light

photocatalytic degradation of waterborne pollutants. *ACS Applied Nano Materials, 2*, 2713–2724.

Kim, P., Park, Y., Ji, K., Seo, J., Lee, S., Choi, K., Kho, Y., Park, J., & Choi, K. (2012). Effect of chronic exposure to acetaminophen and lincomycin on Japanese medaka (Oryzias latipes) and freshwater cladocerans Daphnia magna and Moina macrocopa, and potential mechanisms of endocrine disruption. *Chemosphere, 89*, 10–18.

Kuldeep, A. R., Dhabbe, R. S. & Garadkar, K. M. (2021). Development of g-C_3N_4-TiO_2 visible active hybrid photocatalyst for the photodegradation of methyl orange. *Research on Chemical Intermediates*, 47, 5155–5174.

Li, K., Sun, M., & Zhang, W. (2018). Polycyclic aromatic compounds-modified graphitic carbon nitride for efficient visible-light-driven hydrogen evolution. *Carbon, 134*, 134–144.

Li, L., Yuan, X., Zhou, Z., Tang, R., Deng, Y., Huang, Y., Xiong, S., Su, L., Zhao, J., & Gong, D. (2022). Research progress of photocatalytic activated persulfate removal of environmental organic pollutants by metal and nonmetal based photocatalysts. *Journal of Cleaner Production., 372*, 133420.

Lim, J. K., Sieland, D.-Y., Kim, F., Bahnemann, C., Choi, D. W., & Wonyong,. (2018). Visible light-induced catalytic activation of peroxymonosulfate using heterogeneous surface complexes of amino acids on TiO_2. *Applied Catalysis b: Environmental, 225*, 406–414.

Lin, K., & Zhang, Z. (2017). Degradation of bisphenol A using peroxymonosulfate activated by one-step prepared sulfur-doped carbon nitride as a metal-free heterogeneous catalyst. *Chemical Engineering Journal, 313*, 1320–1327.

Lin, L., Ou, H., Zhang, Y., & Wang, X. (2016). Tri-s-triazine-based crystalline graphitic carbon nitrides for highly efficient hydrogen evolution photocatalysis. *ACS Catalysis, 6*, 3921–3931.

Matzek, L. W., & Carter, K. E. (2016). Activated persulfate for organic chemical degradation: A review. *Chemosphere, 151*, 178–188.

Ming, H., Zhang, P., Yang, Y., Zou, Y., Yang, C., Hou, Y., Ding, K., Zhang, J., & Wang, X. (2022). Tailored polyheptazine units in carbon nitride for activating peroxymonosulfate to degrade organic contaminants with visible light. *Applied Catalysis B: Environmental., 311*, 121341.

Pelaez, M., Nolan, N. T., Pillai, S. C., Seery, M. K., Falaras, P., Kontos, A. G., Dunlop, P. S. M., Hamilton, J. W. J., Byrne, J. A., O'Shea, K., Entezari, M. H., & Dionysiou, D. D. (2012). A review on the visible light active titanium dioxide photocatalysts for environmental applications. *Applied Catalysis b: Environmental, 125*, 331–349.

Piao, H., & McIntyre, N. S. (2002). Adventitious carbon growth on aluminium and gold-aluminium alloy surfaces. *Surface and Interface Analysis, 33*, 591–594.

Saputra, E., Muhammad, S., Sun, H., Ang, H.-M., & Tad, eacute, M. O. & Wang, S. (2013). Manganese oxides at different oxidation states for heterogeneous activation of peroxymonosulfate for phenol degradation in aqueous solutions. *Applied Catalysis b: Environmental, 142–143*, 729–735.

Sudrajat, H. (2018). A one-pot, solid-state route for realizing highly visible light active Na-doped gC_3N_4 photocatalysts. *Journal of Solid State Chemistry, 257*, 26–33.

Tan, S., Xing, Z., Zhang, J., Li, Z., Wu, X., Cui, J., Kuang, J., Zhu, Q., & Zhou, W. (2018a). Ti^{3+}-TiO_2/g-C_3N_4 mesostructured nanosheets heterojunctions as efficient visible-light-driven photocatalysts. *Journal of Catalysis, 357*, 90–99.

Tan, Y., Shu, Z., Zhou, J., Li, T., Wang, W., & Zhao, Z. (2018b). One-step synthesis of nanostructured g-C_3N_4/TiO_2 composite for highly enhanced visible-light photocatalytic H_2 evolution. *Applied Catalysis b: Environmental, 230*, 260–268.

Tao, Y., Ni, Q., Wei, M., Xia, D., Li, X., & Xu, A. (2015). Metal-free activation of peroxymonosulfate by g-C_3N_4 under visible light irradiation for the degradation of organic dyes. *RSC Advances, 5*, 44128–44136.

Tian, D., Zhou, H., Zhang, H., Zhou, P., You, J., Yao, G., Pan, Z., Liu, Y., & Lai, B. (2022). Heterogeneous photocatalyst-driven persulfate activation process under visible light irradiation: From basic catalyst design principles to novel enhancement strategies. *Chemical Engineering Journal., 428*, 131166.

Waclawek, S., Lutze, H., Grubel, K., Padil, V., Cernik, M., & Dionysiou, D. (2017). Chemistry of persulfates in water and wastewater treatment: A review. *Chemical Engineering Journal, 330*, 44–62.

Wang, J., & Wang, S. (2018). Activation of persulfate (PS) and peroxymonosulfate (PMS) and application for the degradation of emerging contaminants. *Chemical Engineering Journal, 334*, 1502–1517.

Wang, Y., Yang, W., Chen, X., Wang, J., & Zhu, Y. (2018). Research paper photocatalytic activity enhancement of core-shell structure g-C_3N_4@TiO_2 via controlled ultrathin g-C_3N_4 layer. *Applied Catalysis b: Environmental, 220*, 337–347.

Wang, Z., Deng, D., & Yang, L. (2014). Degradation of dimethyl phthalate in solutions and soil slurries by persulfate at ambient temperature. *Journal of Hazardous Materials, 271*, 202–209.

Xu, H., Wang, D., Ma, J., Zhang, T., Lu, X., & Chen, Z. (2018). A superior active and stable spinel sulfide for catalytic peroxymonosulfate oxidation of bisphenol S. *Applied Catalysis b: Environmental, 238*, 557–567.

Yang, L., Bai, X., Shi, J., Du, X., Xu, L., & Jin, P. (2019). Quasi-full-visible-light absorption by D35-TiO_2/g-C_3N_4 for synergistic persulfate activation towards efficient photodegradation of micropollutants. *Applied Catalysis B: Environmental., 256*, 117759.

Yang, Q., Ma, Y., Chen, F., Yao, F., Sun, J., Wang, S., Yi, K., Hou, L., Li, X., & Wang, D. (2019). Recent advances in photo-activated sulfate radical-advanced oxidation process (SR-AOP) for refractory organic pollutants removal in water. *Chemical Engineering Journal., 378*, 122149.

Yang, Y., Guo, Y., Liu, F., Yuan, X., Guo, Y., Zhang, S., Guo, W., & Huo, M. (2013). Preparation and enhanced visible-light photocatalytic activity of silver deposited graphitic carbon nitride plasmonic photocatalyst. *Applied Catalysis b: Environmental, 142–143*, 828–837.

Zada, A., Qu, Y., Ali, S., Sun, N., Lu, H., Yan, R., Zhang, X., & Jing, L. (2018). Improved visible-light activities for degrading pollutants on TiO2/g-C3N4 nanocomposites by decorating SPR Au nanoparticles and

2,4-dichlorophenol decomposition path. *Journal of Hazardous Materials, 342*, 715–723.

Zhang, G., Sun, Y., Zhang, C., & Yu, Z. (2017). Decomposition of acetaminophen in water by a gas phase dielectric barrier discharge plasma combined with TiO_2-rGO nanocomposite: Mechanism and degradation pathway. *Journal of Hazardous Materials, 323*, 719–729.

Zhang, L., Hu, J., Zhu, R., Zhou, Q., & Chen, J. (2013). Degradation of paracetamol by pure bacterial cultures and their microbial consortium. *Applied Microbiology & Biotechnology, 97*, 3687–3698.

Zhang, L., Yin, X., & Li, S. F. Y. (2015). Bio-electrochemical degradation of paracetamol in a microbial fuel cell-Fenton system. *Chemical Engineering Journal, 276*, 185–192.

Zhang, S., Song, S., Gu, P., Ma, R., Wei, D., Zhao, G., Wen, T., Jehan, R., Hu, B., & Wang, X. (2019a). Visible-light-driven activation of persulfate over cyano and hydroxyl group co-modified mesoporous g-C3N4 for boosting bisphenol A degradation. *Jouranl of Materials Chemistry A, 7*, 5552–5560.

Zhang, T., Liu, Y., Rao, Y., Li, X., Yuan, D., Tang, S., & Zhao, Q. (2020). Enhanced photocatalytic activity of TiO_2 with acetylene black and persulfate for degradation of tetracycline hydrochloride under visible light. *Chemical Engineering Journal., 384*, 123350.

Zhang, Y., Xiao, Y., Zhong, Y., & Lim, T.-T. (2019b). Comparison of amoxicillin photodegradation in the UV/H_2O_2 and UV/persulfate systems: Reaction kinetics, degradation pathways, and antibacterial activity. *Chemical Engineering Journal, 372*, 420–428.

Zhou, G., Sun, H., & Wang, S. (2011). Titanate supported cobalt catalysts for photochemical oxidation of phenol under visible light irradiations. *Separation and Purification Technology, 80*, 626–634.

Zhou, H., Lai, L., Wan, Y., He, Y., Yao, G., & Lai, B. (2020). Molybdenum disulfide (MoS_2): A versatile activator of both peroxymonosulfate and persulfate for the degradation of carbamazepine. *Chemical Engineering Journal., 384*, 123264.

Zhou, L., Zhang, H., Sun, H., Liu, S., Tade, M., Wang, S., & Jin, W. (2016). Recent advances in non-metal modification of graphitic carbon nitride for photocatalysis: A historic review. *Catalysis Science & Technology, 6*, 7002–7023.

Zhou, Z., Liu, X., Sun, K., Lin, C., Ma, J., He, M., & Ouyang, W. (2019). Persulfate-based advanced oxidation processes (AOPs) for organic-contaminated soil remediation: A review. *Chemical Engineering Journal, 372*, 836–851.

Zou, X., Sun, Z., & Hu, Y. (2020). g-C3N4-based photoelectrodes for photoelectrochemical water splitting: A review. *Journal of Materials Chemistry A, 8*, 21474–21502.